



## Hexagonal $\text{Sr}_{1-x/2}\text{Al}_{2-x}\text{Si}_x\text{O}_4:\text{Eu}^{2+}, \text{Dy}^{3+}$ transparent ceramics with tuneable persistent luminescence properties

Victor Castaing, Charlotte Monteiro, Atul D Sontakke, Kazuki Asami, Jian Xu, Alberto J Fernández Carrión, Mikhail G Brik, Setsuhisa Tanabe, Mathieu Allix, Bruno Viana

### ► To cite this version:

Victor Castaing, Charlotte Monteiro, Atul D Sontakke, Kazuki Asami, Jian Xu, et al.. Hexagonal  $\text{Sr}_{1-x/2}\text{Al}_{2-x}\text{Si}_x\text{O}_4:\text{Eu}^{2+}, \text{Dy}^{3+}$  transparent ceramics with tuneable persistent luminescence properties. Dalton Transactions, 2020, 10.1039/D0DT03137B . hal-03023630

**HAL Id: hal-03023630**

**<https://hal.science/hal-03023630>**

Submitted on 25 Nov 2020

**HAL** is a multi-disciplinary open access archive for the deposit and dissemination of scientific research documents, whether they are published or not. The documents may come from teaching and research institutions in France or abroad, or from public or private research centers.

L'archive ouverte pluridisciplinaire **HAL**, est destinée au dépôt et à la diffusion de documents scientifiques de niveau recherche, publiés ou non, émanant des établissements d'enseignement et de recherche français ou étrangers, des laboratoires publics ou privés.

# Hexagonal $\text{Sr}_{1-x/2}\text{Al}_{2-x}\text{Si}_x\text{O}_4\text{:Eu}^{2+},\text{Dy}^{3+}$ transparent ceramics with tuneable persistent luminescence properties

Victor Castaing<sup>a,\*</sup>, Charlotte Monteiro<sup>b</sup>, Atul D. Sontakke<sup>a, c</sup>, Kazuki Asami<sup>d</sup>, Jian Xu<sup>d</sup>, Alberto J. Fernández Carrión<sup>b, e</sup>, Mikhail G. Brik<sup>f</sup>, Setsuhisa Tanabe<sup>d</sup>, Mathieu Allix<sup>b</sup> and Bruno Viana<sup>a,\*</sup>.

Received 00th January 20xx,  
Accepted 00th January 20xx

DOI: 10.1039/x0xx00000x

www.rsc.org/

Co-doped hexagonal  $\text{Sr}_{1-x/2}\text{Al}_{2-x}\text{Si}_x\text{O}_4\text{:Eu}^{2+},\text{Dy}^{3+}$  ( $0.1 \leq x \leq 0.5$ ) transparent ceramics have been elaborated by full glass crystallization. The compositions with low  $\text{SiO}_2$  content ( $x \leq 0.4$ ) require fast quenching conditions to form glass, *i.e.* specific elaboration processes such as aerodynamic levitation coupled to laser heating, whereas the  $x=0.5$  glass composition can be prepared at large scale by classic melt-quenching method in commercial furnaces. After a single thermal treatment, the resulting  $\text{SrAl}_2\text{O}_4$ -based transparent ceramics show varying photoluminescence emission properties when  $x$  increases. These variations are also observable in persistent luminescence, resulting in an afterglow colour-tuning ranging from green to light blue. Afterglow excitation spectra highlight the possible activation in the visible range of the obtained persistent luminescence. Indeed, persistent luminescence of hexagonal  $\text{Sr}_{0.75}\text{Al}_{1.5}\text{Si}_{0.5}\text{O}_4\text{:Eu}^{2+},\text{Dy}^{3+}$  large transparent ceramics has been successfully charged using a typical smartphone low power white light source. Moreover, thermoluminescence glow curves of samples containing different  $\text{Dy}^{3+}$  doping concentrations are studied to gain insights regarding the traps origin and depth. Coupling thermoluminescence results together with luminescence thermal quenching and band gap calculations appears useful to understand the charge trapping and detrapping evolution with the material composition. Varying the Si-content in hexagonal  $\text{Sr}_{1-x/2}\text{Al}_{2-x}\text{Si}_x\text{O}_4\text{:Eu}^{2+},\text{Dy}^{3+}$  compounds appears as a promising strategy to obtain transparent materials with tuneable green to light blue persistent luminescence.

## 1. Introduction

Energy storage phosphors, particularly the persistent phosphors, have been widely studied in the past twenty years aiming at the elaboration of the next generation of lighting materials. These materials are able to store so-called optical energy, mostly UV, and emit light for minutes to hours after the excitation stoppage. The applications cover wide ranges from emergency lighting, safety signs, visualization, decorations, etc. Extensive research on these particular materials started after the discovery of the  $\text{SrAl}_2\text{O}_4\text{:Eu}^{2+},\text{Dy}^{3+}$  phosphor by Matsuzawa *et al.*, demonstrating considerably intense and long green afterglow emission<sup>1</sup> arising from the  $5d \rightarrow 4f$  transition of the  $\text{Eu}^{2+}$  doping ion. This famous material, as well as the well-known  $\text{CaAl}_2\text{O}_4\text{:Eu}^{2+},\text{Nd}^{3+}$ , have been elaborated by different techniques<sup>2–5</sup> and widely studied<sup>6–15</sup> to better understand their persistent luminescence mechanism.

Since then, many other materials have been elaborated and studied with that purpose.<sup>16,17</sup> Amongst others, garnets ( $\text{Y}_3\text{Al}_2\text{Ga}_3\text{O}_{12}\text{:Ce}^{3+},\text{Cr}^{3+}$ ,  $\text{Gd}_3\text{Al}_2\text{Ga}_3\text{O}_{12}\text{:Ce}^{3+},\text{Cr}^{3+}$ ), perovskite-type niobates or titanates ( $\text{NaNbO}_3\text{:Pr}^{3+}$ ,  $\text{CaTiO}_3\text{:Pr}^{3+}$ ) and spinel gallates ( $\text{ZnGa}_2\text{O}_4\text{:Cr}^{3+}$ ,  $\text{Zn}_{1.1}\text{Ga}_{1.8}\text{Ge}_{0.1}\text{O}_4\text{:Cr}^{3+}$ ) are famous persistent luminescence materials.<sup>18–26</sup> However, most of these persistent materials require UV irradiation to be charged. This is a noteworthy obstacle for most of the targeted applications. Indeed, the most convenient and common excitation sources are the sunlight and white light-emitting diodes (w-LEDs), which mostly provide visible light. Therefore, in view of widespread usage, persistent luminescence materials chargeable with visible light illumination become more advantageous.

At present, most ceramic persistent phosphors are used as security signage when incorporated in paints. The painted writings or signs can thus be seen for hours after the dark is set. Yet, even though they already find usage as cycling or jogging lanes illumination during night time, the persistent phosphors require improved performance for large area lighting applications.<sup>27,28</sup> Designing transparent bulk persistent phosphors then appears as a promising strategy to overcome the intensity weakness of the materials due to lower light scattering than in the powder phosphor case. Such an approach would enable persistent charging and emission from the whole material volume, thus effectively reducing energy loss.<sup>18</sup> This “volume effect” was demonstrated by Xu *et al.* in  $\text{YAGG}\text{:Ce}^{3+},\text{Cr}^{3+}$  where an effective improvement of the persistent decay was induced by increasing the transparent ceramic thickness.<sup>19</sup> Moreover, such designs allow reading through the transparent persistent phosphor thereby using the material as a lighting screen.<sup>29</sup> In

<sup>a</sup> Chimie ParisTech, Institut de Recherche de Chimie Paris, PSL Research University, CNRS, Paris 75005, France

<sup>b</sup> CNRS, CEMHTI UPR3079, Université Orléans, F-45071 Orléans, France

<sup>c</sup> Condensed Matter & Interfaces, Debye Institute for Nanomaterials Science, Utrecht University, Princetonplein 1, 3584 CC Utrecht, The Netherlands

<sup>d</sup> Graduate School of Human and Environmental Studies, Kyoto University, Kyoto 606-8501, Japan

<sup>e</sup> MOE Key Laboratory of New Processing Technology for Nonferrous Metals and Materials, Guangxi Universities Key Laboratory of Non-ferrous Metal Oxide Electronic Functional Materials and Devices, College of Materials Science and Engineering, Guilin University of Technology, Guilin 541004, P. R. China

<sup>f</sup> Institute of Physics, University of Tartu, W. Ostwald Str. 1, Tartu, 50411, Estonia  
E-mail: victor.castaing@chimieparistech.psl.eu  
bruno.viana@chimieparistech.psl.eu

view of such added capabilities compared to glow in the dark inks, transparent persistent phosphors show potential advantages for security and night vision applications.

Moreover, current available afterglow emission colours are fairly limited. This is due to the fact that persistent emission properties mostly arise from one of the doping ions located in a particular crystalline compound type, mostly giving access to dark blue ( $\text{Eu}^{2+}$  in  $\text{CaAl}_2\text{O}_4\text{:Eu}^{2+},\text{Nd}^{3+}$ ) and green ( $\text{Eu}^{2+}$  in  $\text{SrAl}_2\text{O}_4\text{:Eu}^{2+},\text{Dy}^{3+}$ ) persistent emissions. Widening the colour range, giving access to a higher contrast using association of persistent materials with different colours, is of major interest for signalization applications. For that purpose, the most common strategy is to modify the host matrix to change the crystal field strength on the emitting cation and shifts its emission. The elaboration of materials with combined persistent emission centres gathered in a single-phase phosphor appears as another promising direction to create a broad range of persistent luminescence colours though less studied. Only few phosphors with persistent luminescence arising from combined emission centres, based on persistent energy transfers, have been reported.<sup>30,31</sup>

Several recently developed persistent phosphors achieve one or two of these criteria, in particular some persistent garnets that are transparent and can be efficiently charged by visible light.<sup>18,19</sup> Within this work, we aimed at elaborating and characterizing a material fulfilling the three above cited criteria *i.e.* a transparent persistent ceramic monolith with colour tuneability excited by visible light.

Recently, full crystallization of glass was presented as a promising process to synthesize innovative transparent ceramics.<sup>32–41</sup> Among the several transparent materials developed, the metastable solid-solution  $\text{Sr}_{1-x/2}\text{Al}_{2-x}\text{Si}_x\text{O}_4$  (h-SASO  $x$  with  $0.2 \leq x \leq 0.5$ ) presents tuneable luminescence properties when doped with europium.<sup>42,43</sup> Given that its structure derives from the hexagonal polymorph of  $\text{SrAl}_2\text{O}_4$ , which is reported to have persistent luminescence properties,<sup>44</sup> this solid-solution appears promising to tune the famous properties of the monoclinic  $\text{SrAl}_2\text{O}_4\text{:Eu}^{2+},\text{Dy}^{3+}$  persistent phosphor. Indeed, due to a combination of absence of porosity, crystallite orientation (birefringent structure) and optical isotropy induced by structural disorder, the materials belonging to the  $\text{Sr}_{1-x/2}\text{Al}_{2-x}\text{Si}_x\text{O}_4$  solid solution show a remarkable transparency.  $\text{Sr}^{2+}$  cations occupy different crystallographic sites in the two  $\text{SrAl}_2\text{O}_4$  polymorphs. In the monoclinic structure, two  $\text{Sr}^{2+}$  sites exist whereas in the hexagonal structure five different  $\text{Sr}^{2+}$  sites can be found.<sup>42</sup> As  $\text{Eu}^{2+}$  substitutes for  $\text{Sr}^{2+}$ , different optical properties can be observed for the two polymorphs.<sup>42,45</sup> Moreover, as the Sr sites occupancies evolve along the solid solution, tuneable persistent luminescence properties can be expected.

In the present study, we report the elaboration of hexagonal  $\text{Sr}_{1-x/2}\text{Al}_{2-x}\text{Si}_x\text{O}_4\text{:Eu}^{2+},\text{Dy}^{3+}$  (h-SASO  $x$ , with  $0.1 \leq x \leq 0.5$ ) transparent ceramics. Their optical properties, among which persistent luminescence, are studied in detail and compared to each other along the solid solution. Finally, the luminescence properties evolution is discussed based on experimental results, on semi-empirical model and on density functional theory calculations.

## 2. Experimental procedures

### 2.1. Synthesis.

In this study, compositions  $\text{Sr}_{1-x/2}\text{Al}_{2-x}\text{Si}_x\text{O}_4$  where  $x = 0, 0.05, 0.08, 0.09, 0.1, 0.2, 0.3, 0.4$  and  $0.5$  were investigated and were either

single-doped by  $\text{Eu}^{2+}$  (1%  $\text{Eu}^{2+}$  in substitution to Sr) or co-doped with  $\text{Eu}^{2+}$ ,  $\text{Dy}^{3+}$  (1 %  $\text{Eu}^{2+}$  and 2 %  $\text{Dy}^{3+}$ ). Moreover, for the  $x = 0.5$  compound, a series of  $\text{Dy}^{3+}$  contents varying from 0 % to 5 % were investigated. Melting of each composition has been performed using a double  $\text{CO}_2$  laser-heating system coupled to an aerodynamic levitation (ADL) system.<sup>46,47</sup> High purity  $\text{SrCO}_3$  (99.9%, Strem Chemicals),  $\text{Al}_2\text{O}_3$  (99.98%, Alfa Aesar),  $\text{SiO}_2$  (99.999%, Strem Chemicals),  $\text{Eu}_2\text{O}_3$  (99.99%, Sigma Aldrich) and  $\text{Dy}_2\text{O}_3$  (99.99%, Alfa Aesar) precursors were first weighed in stoichiometric amounts and mixed in an agate mortar with absolute ethanol. Each powder batch was then pressed into pellets and placed on a metallic nozzle. Aerodynamic levitation was ensured using an argon gas flow. Depending on the composition, temperatures used for melting were ranging from ca. 1900 °C to 1700 °C (the melting temperature decreases with the increase of the Si-content).  $0 \leq x \leq 0.09$  compositions could not be entirely vitrified as crystallisation systematically occurred directly during quenching from the melt. For  $x = 0.1$  composition, only 1 mm diameter beads could be vitrified. Nevertheless, 3 mm diameter glass beads could be obtained for compositions with  $0.2 \leq x \leq 0.5$  by free cooling down to room temperature after laser heating stoppage.

For the  $x = 0.5$  sample, glass could also be obtained at much larger scale, with a maximum of 10 g of the mixed precursors, using classical melt-quenching method in a Pt crucible at 1750 °C. The crystallization stage of the glassy samples was subsequently conducted as reported by Fernández-Carrión *et al.* ( $T_{\text{cryst}} = 975$  °C for 7 h), excepted that the heating atmosphere was turned into reducing atmosphere ( $\text{H}_2/\text{N}_2$  mixing, 5 % of  $\text{H}_2$ ) to promote europium reduction.<sup>42</sup>

### 2.2. Structure and optical properties characterizations.

X-ray powder diffraction data were recorded using a Bragg-Brentano D8 Advance Bruker diffractometer (Cu K $\alpha$  radiation) equipped with a LynxEye XE detector over an angular range of  $19^\circ < 2\theta < 70^\circ$  using a  $0.020^\circ$  step size.

An optical parametric oscillator (OPO) pulsed laser has been used for the excitation of photoluminescence (PL) measurements while the acquisition was held by a CCD camera (Princeton Instruments, PI-MAX 4) coupled to a monochromator (Princeton Instruments, Acton SP 2300). For photoluminescence excitation (PLE) and temperature dependence of PL/PLE, the excitation was provided by a white lamp (EQ-99X LDLS, ENERGETIQ) coupled to a visible monochromator. LEDs (ThorLabs) were used to excite samples for persistent emission measurements. A typical smartphone white light emitting diode (w-LED, placed 10 cm away from the sample, giving an illuminance of 2740 Lux) was also used to activate persistent luminescence. Persistent decay glow curves were obtained by integrating persistent emission intensity as a function of time. For radiance decay measurements, the samples were charged using a 300 W Xe lamp (Asahi) attached with the UV module (centred at 330 nm) for 5 minutes at 25 °C. Then, the persistent emission decay was recorded using a photomultiplier tube (R11041, Hamamatsu Photonics) coupled with calibrated photodiode detector (S-025-H, Electro-Optical System Inc.) for absolute radiance conversion. Persistent excitation spectra were obtained by integrating persistent luminescence intensity after 1 min excitation at each wavelength step obtained using a white lamp (EQ-99X LDLS, ENERGETIQ) coupled to a visible monochromator. Thermoluminescence measurements were carried out using a closed-cycle He-flow cryostat (Sumitomo Cryogenics HC-4E) attached with a Lakeshore 340 temperature controller. The samples were cooled to 13 K and irradiated using a 365 nm UV lamp (Vilber Lourmat,

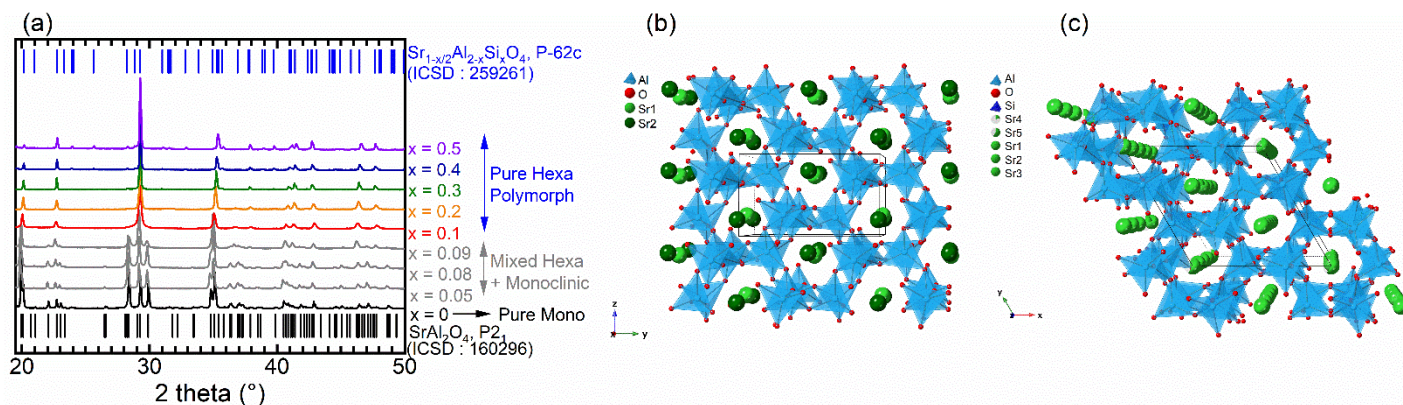


**Fig. 1.** (a) X-ray powder diffraction (XRPD) patterns of  $\text{Sr}_{1-x/2}\text{Al}_{2-x}\text{Si}_x\text{O}_4:\text{Eu}^{2+},\text{Dy}^{3+}$  ceramics obtained with the melt quenching technique followed by a second heat treatment stage. The  $x = 0$  sample crystallized directly from the melt. Samples with  $0 < x < 0.1$  partially crystallized from the melt whereas glasses were obtained for  $0.1 \leq x \leq 0.5$  compositions. After the second heat treatment stage all the samples are completely crystallized. The  $x = 0$  sample corresponds to the monoclinic polymorph whereas the  $0.1 \leq x \leq 0.5$  compositions crystallize in the pure hexagonal polymorph. (b) Monoclinic  $\text{SrAl}_2\text{O}_4$  and (c) hexagonal  $\text{Sr}_{0.8}\text{Al}_{1.6}\text{Si}_{0.4}\text{O}_4$  crystal lattices in which Sr, Al, Si, O atoms and vacancies are represented by green, light blue, dark blue, red and white spheres, respectively.

Hg vapor lamp) for five minutes. Subsequently, after a waiting time of one minute, the thermoluminescence glow curves were recorded at  $10^\circ\text{C}\cdot\text{min}^{-1}$  ramp rate from 13 K to 600 K. For the sake of comparison, a TL glow curve has been recorded with charging at 273 K, cooling down to 213 K with the same heating ramp. In these experiments, the signals were recorded by a CCD camera (Roper Pixis 100) coupled to a visible monochromator (Acton Spectra Pro, Princeton Instruments, 300 grooves per mm, centred at 600 nm).

### 2.3. Theoretical calculations.

The density functional theory (DFT) calculations of the structural and electronic properties of  $\text{Sr}_{1-x/2}\text{Al}_{2-x}\text{Si}_x\text{O}_4$  ( $x = 0, 0.2$  and  $0.5$ ) were performed using the CASTEP module of Materials Studio 2017<sup>48</sup> package and the GGA-PBE functionals.<sup>49</sup> The ionic core electrons were replaced by on-the-fly ultrasoft pseudopotentials implemented in the CASTEP with the following electronic configurations: [Kr]  $4s^2 4p^6 5s^2$  for Sr, [Ne]  $3s^2 3p^1$  for Al, [Ne]  $3s^2 3p^2$  for Si and [He]  $2s^2 2p^4$  for O.<sup>50</sup> Relativistic effects were taken into account at the level of the Koelling-Harmon approximation of the Dirac equation.<sup>44</sup> The plane-wave basis energy cut-off was chosen as 630.0 eV and  $k$ -point grids were chosen as  $3 \times 2 \times 2$  for  $x = 0$  and  $2 \times 2 \times 2$  for  $x = 0.2$  and  $0.5$ . The convergence parameters were as follows: total energy tolerance  $5.0 \times 10^{-6}$  eV/atom, maximum force tolerance 0.01 eV/Å, maximum stress component 0.02 GPa and maximum displacement  $5.0 \times 10^{-4}$  Å.

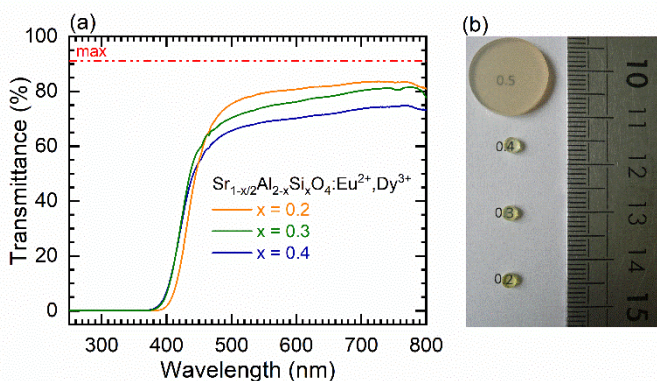


**Fig. 2.** (a) Spectral dependence of the transmittance of the as elaborated h-SASO samples. (b) Photographs of the corresponding transparent ceramics. The scale bar is in cm scale (the small samples are 1.6 mm thick whereas the  $x = 0.5$  sample is 2.2 mm thick).

## 3. Results and discussion

### 3.1. Crystal structure and morphology.

The nature of the crystallized singly-doped and co-doped samples was first checked by X-ray diffraction, see Figure 1(a). For the  $x = 0$  sample, the crystalline phase was obtained directly by cooling from the melt which was attributed to the cooling rate of aerodynamic levitation (*ca.* 300–500  $^\circ\text{C}$  per second) which is not high enough to ensure glass formation of  $\text{SrAl}_2\text{O}_4$ . The resulting crystalline phase can be indexed by the monoclinic polymorph of  $\text{SrAl}_2\text{O}_4$  (PDF 01-076-7488), without any additional trace of  $\text{Eu}_2\text{O}_3$  nor  $\text{Dy}_2\text{O}_3$ . For  $0 < x < 0.1$ , partial crystallization was obtained by cooling from the melt (some unwanted crystallization could not be avoided). However, unlike the  $x = 0$  material, after the subsequent heat treatment, both monoclinic and hexagonal polymorphs are formed, with an increasing ratio of hexagonal polymorph when the  $x$  value increases. The two crystalline structures are represented on Figure 1(b) and (c) respectively. From XRPD patterns comparison, it is clear that the Si substitution for Al (and the associated Sr vacancy increase) promotes the hexagonal polymorph stabilization, as demonstrated by the increasing content of hexagonal polymorph as  $x$  increases (ICSD 259261, 259262 and 259263).<sup>42</sup> Finally, for higher Si contents ( $x \geq 0.1$ ), glass formation was possible and polycrystalline ceramics could be obtained *via* full glass crystallization after subsequent thermal treatment. No trace of monoclinic- $\text{SrAl}_2\text{O}_4$  polymorph,  $\text{Eu}_2\text{O}_3$ , nor  $\text{Dy}_2\text{O}_3$  phases could be observed for these compositions. A shift of the diffraction peaks towards higher diffraction angles is observed all along the series, which can be explained by lattice contraction along the substitution of  $\text{Al}^{3+}$  (0.39 Å) by a smaller cation  $\text{Si}^{4+}$  (0.26 Å) and the increase of  $\text{Sr}^{2+}$  vacancies.<sup>52</sup> In these  $\text{SrAl}_2\text{O}_4:\text{Eu}^{2+},\text{Dy}^{3+}$  materials,  $\text{Eu}^{2+}$  and  $\text{Dy}^{3+}$  are expected to substitute for  $\text{Sr}^{2+}$ . Indeed, these rare earth cations have excessive large radius difference with  $\text{Al}^{3+}$ , well beyond the limit of the Hume-Rothery atomic substitution rule. Moreover, no amorphous phase could be observed from X-ray diffraction and electron microscopy, suggesting that full crystallization occurs in these materials.

As reported for their  $\text{Eu}^{2+}$  singly doped counterparts, the ceramic samples show good transparency in the visible range (see Figure 2).<sup>42</sup> Note that the  $x = 0.1$  sample is not shown here as glass crystallization could not be performed without the appearance of



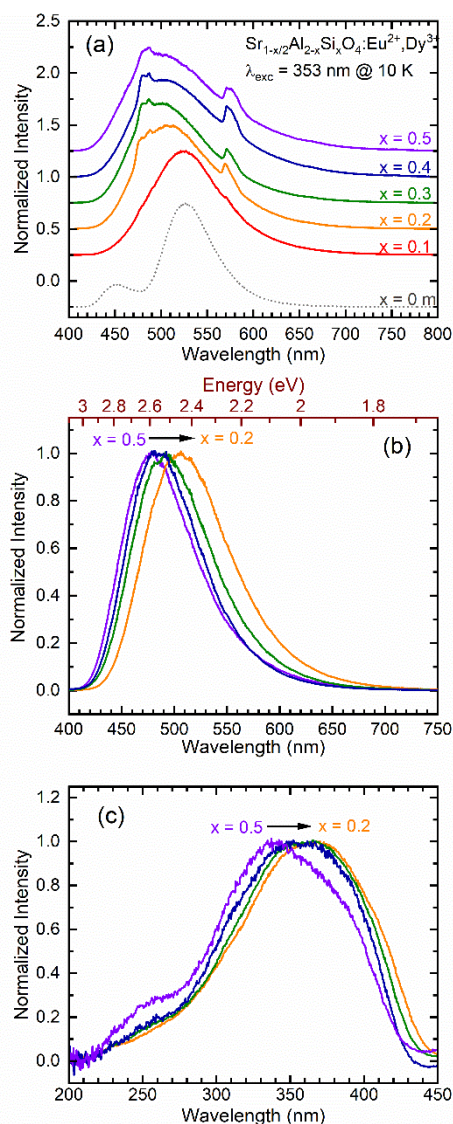


**Fig. 3.** (a) Normalized emission spectra ( $\lambda_{\text{exc}} = 353 \text{ nm}$ ) of hexagonal  $\text{Sr}_{1-x/2}\text{Al}_{2-x}\text{Si}_x\text{O}_4: 1\% \text{ Eu}^{2+}, 2\% \text{ Dy}^{3+}$  ( $x$  ranging from 0.1 to 0.5) recorded at 10 K. Monoclinic  $\text{SrAl}_2\text{O}_4:\text{Eu}^{2+}, \text{Dy}^{3+}$  emission recorded in the same conditions is also displayed for comparison. (b) Emission spectra of the  $\text{Eu}^{2+}$  singly doped samples recorded at 10 K plotted with energy scale. (c) RT excitation spectra of the co-doped samples.

cracks for this composition. This can be linked to the small size (diameter of 1 mm) of the initial glass beads, which makes very difficult the crystallization process control of these samples. The observed yellow tint of the ceramics can be linked with the blue absorption of  $\text{Eu}^{2+}$  observed until ca. 450 nm. Above this region, the transparency of the samples is very high in the visible range, reaching 83 % for  $\text{Sr}_{0.9}\text{Al}_{1.8}\text{Si}_{0.2}\text{O}_4:\text{Eu}^{2+}, \text{Dy}^{3+}$  (see Figure 2(a)). From a glass forming point of view, it can be observed that the synthesis temperature (temperature used to vitrify each composition) decreases when the Si-content ( $x$ ) increases (see Fig. S1). As the glass formation is eased when the Si-content ( $x$ ) increases, it is thus possible to elaborate the  $x = 0.5$  glass composition using a commercial furnace (synthesis temperature of about 1750°C using a Pt/Rh crucible), enabling much larger scale samples to be synthesized (the size of the  $x = 0.5$  sample presented figure 2(b) was limited by size of our platinum crucible).

### 3.2. Photoluminescence properties

As previously established on monoclinic- $\text{SrAl}_2\text{O}_4:\text{Eu}^{2+}, \text{Dy}^{3+}$  materials elaborated *via* different methods, two broad PL bands arising from the two distinct Sr crystallographic sites appear at low temperature on the  $x = 0$  sample: one blue and one green located at ca. 450 nm and 530 nm respectively (Figure 3(a)).<sup>45,53</sup> Unlike this well studied material, the hexagonal  $\text{Sr}_{1-x/2}\text{Al}_{2-x}\text{Si}_x\text{O}_4:\text{Eu}^{2+}, \text{Dy}^{3+}$  ( $x > 0$ ) compounds show one broad band and two relatively narrow bands, see Figure 3(a). The main band appears much broader compared to the monoclinic material, ranging from ca. 420 nm to 700 nm. Due to its broad shape and spectral position, the central broad band can be related to the  $\text{Eu}^{2+}$  emission. This broad band evolves as  $x$  increases. Indeed, increasing the Si substitution for Al and the Sr vacancies content induces a shift of the  $\text{Eu}^{2+}$  signal towards higher energies. It is not surprising that the  $\text{Eu}^{2+}$  emission band changes with the counter cation nature ( $\text{Al}^{3+}$  and  $\text{Si}^{4+}$ ) as its emission arises from the  $4f^65d^1 \rightarrow 4f^7$  transition and d orbitals are known to be sensitive to the local environment, due to several effects such as crystal field splitting and centroid shift.<sup>54</sup>

To go further, photoluminescence measurements have been performed at low temperature (10 K) on  $\text{Eu}^{2+}$  singly doped h-SASO samples with different compositions ( $x$  varying from 0.2 to 0.5). The  $\text{Eu}^{2+}$  singly doped hexagonal  $\text{Sr}_{0.95}\text{Al}_{1.9}\text{Si}_{0.1}\text{O}_4$  ( $x = 0.1$ ) ceramic has not been studied here, as the glass precursor could not be prepared without  $\text{Dy}^{3+}$  (no single Eu-doped glass could be formed by ADL). The resulting emission spectra, presented in Figure 3(b), exhibit a broad band with an asymmetric shape. As previous structural investigations of the h-SASO materials revealed the existence of five different Sr crystallographic sites,  $\text{Eu}^{2+}$  emission arising from multiple  $\text{Eu}^{2+}$  centers can be expected. Actually, to compensate positively charged defects induced by  $\text{Si}^{4+}$  substitution for  $\text{Al}^{3+}$  ( $\text{Si}_{\text{Al}}^{\bullet}$ ), Sr vacancies ( $\text{V}_{\text{Sr}}^{\bullet}$ ) are formed in selective Sr sites (two of the five different Sr sites). Therefore, it appears reasonable to observe an asymmetric broad  $\text{Eu}^{2+}$  emission as the  $\text{Eu}^{2+}$  emissions arising from emitters in different Sr sites may overlap.

Still, a clear blue shift of the  $\text{Eu}^{2+}$  emission band can be clearly seen as  $x$  increases. This blue shift may result from several effects such as the counter cation effect ( $\text{Al}^{3+}$  and  $\text{Si}^{4+}$ ), the effect of  $\text{V}_{\text{Sr}}^{\bullet}$  and its increase with Si content, the decrease of  $\text{Eu}^{2+}$  population in specific sites. The origin of the observed blue shift will be further discussed on the basis of a semi-empirical model.

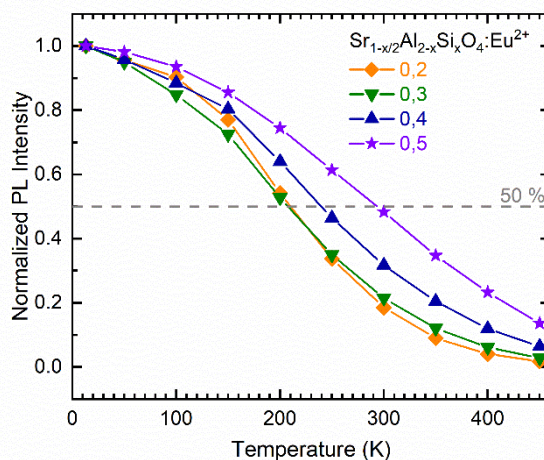


**Fig. 4.** Temperature dependence of the  $\text{Sr}_{1-x/2}\text{Al}_{2-x}\text{Si}_x\text{O}_4:\text{Eu}^{2+}, \text{Dy}^{3+}$  normalized integrated PL intensity ( $\lambda_{\text{exc}} = 353 \text{ nm}$ ).

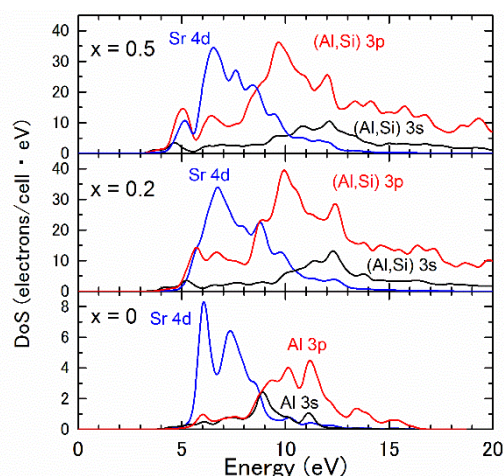


**Fig. 5.** Hexagonal  $\text{Sr}_{1-x/2}\text{Al}_{2-x}\text{Si}_2\text{O}_4$  density of states (from top to bottom,  $x = 0, 0.2$  and  $0.5$ ).

On the contrary, the narrow bands located at *ca.* 488 and 573 nm (Figure 3(a)) show the same spectral position and shape independently from the sample composition ( $x$  value). Given their shapes, spectral positions and consistency with the host, they can be attributed to  $\text{Dy}^{3+}$  4f-4f transitions:  $4\text{F}_{9/2} \rightarrow 6\text{H}_{15/2}$  and  $4\text{F}_{9/2} \rightarrow 6\text{H}_{13/2}$  (488 and 573 nm respectively). In order to validate this assumption, the  $\text{Dy}^{3+}$  doping content has been varied in the  $x = 0.5$  sample (from 0 % to 5 % of  $\text{Dy}^{3+}$ ). On the resulting PL spectra (Fig. S2), the sharp signal contribution is absent for the 0 %  $\text{Dy}^{3+}$  doping content but its intensity rises for the samples ranging from 0.25 % to 5 %  $\text{Dy}^{3+}$ . It is thus reasonable to attribute the sharp lines to  $\text{Dy}^{3+}$  emission. Moreover, the  $\text{Dy}^{3+}$  content variation appears to have no effect on the large band related to  $\text{Eu}^{2+}$ . Interestingly, the intensity of the  $\text{Dy}^{3+}$  band tends to increase compared to the  $\text{Eu}^{2+}$  emission as the Si content ( $x$ ) increases. This is in good agreement with the fact that the  $\text{Eu}^{2+}$  emission shifts towards lower wavelengths with the Si-content. Indeed, due to the blue shift, the  $\text{Eu}^{2+}$   $4\text{f}^65\text{d} \rightarrow 4\text{f}^7$  emission is more overlapped with the absorption bands of  $\text{Dy}^{3+}$   $6\text{H}_{15/2} \rightarrow 4\text{F}_{9/2}$  and  $6\text{H}_{15/2} \rightarrow 4\text{I}_{15/2}$  transitions making the  $\text{Eu}^{2+}$  to  $\text{Dy}^{3+}$  energy transfer more efficient, as schematized in Fig. S3. The apparition and increase of the  $\text{Dy}^{3+}$  emission peaks, combined with the  $\text{Eu}^{2+}$  blue shift lead to an interesting colour change from green to light blue (for  $x = 0.1$  and  $x = 0.5$  respectively).

The co-doped h-SASO excitation spectra, presented in Figure 3(c), appear to be constituted of one broad band with a hump at *ca.* 250 nm. It can be attributed to overlapped  $4\text{f}^7 \rightarrow 4\text{f}^65\text{d}^1$  excitations of  $\text{Eu}^{2+}$ . Moreover, the excitation spectra show the same blue shift as  $x$  increases, which can be assigned to the variation of the  $\text{Eu}^{2+}$  neighbourhood when  $\text{Si}^{4+}$  substitutes for  $\text{Al}^{3+}$  and creates Strontium vacancies. As several  $\text{Eu}^{2+}$  sites are expected in this material, the PLE spectra of h-SASO 0.5 taken at different  $\lambda_{\text{em}}$  have been analysed (Fig. S4). The  $\text{Eu}^{2+}$  excitation spectra recorded at different emissions ( $\lambda_{\text{em}} = 440$  nm and  $\lambda_{\text{em}} = 600$  nm) show very distinct shapes, evidencing that  $\text{Eu}^{2+}$  cations occupy several different sites in the material. On the other hand, PLE spectrum monitoring the  $\text{Dy}^{3+}$  emission ( $\lambda_{\text{em}} = 744$  nm ( $\text{Dy}^{3+}$ :  $4\text{F}_{9/2} \rightarrow 6\text{F}_{11/2}, 6\text{H}_{9/2}$ )) has been plotted (see the PL/PLE plot of the  $x = 0.5$  compound in Fig. S5). The obtained  $\text{Dy}^{3+}$  excitation spectrum is nearly stackable to the  $\text{Eu}^{2+}$  excitation revealing an energy transfer from  $\text{Eu}^{2+}$  to  $\text{Dy}^{3+}$ . Only very weak intensity contribution can be found at *ca.* 453 nm due to the  $\text{Dy}^{3+}$ :  $6\text{H}_{15/2} \rightarrow 4\text{F}_{9/2}$  transition. It is worth noticing that this charging band is not observed during the luminescence excitation of  $\text{Eu}^{2+}$ , even with

higher  $\text{Dy}^{3+}$  contents (Fig. S6). This reveals that no reversible energy transfer can be observed in these materials.

To get insights on the  $\text{Eu}^{2+}$  excitation shift with the materials composition, a semi-empirical model has been studied (see Supporting Information S7). In this model, the  $\text{Eu}^{2+}$  redshift is explained as a combination of the crystal field splitting and the centroid shift. As previously defined by P. Dorenbos and studied in the supplementary information, the crystal field splitting in our materials should depend on the average Eu-O distances and the centroid shift on the effective Eu-O distances as well as on the spectroscopic polarizability.<sup>55–58</sup>

The evolution of the effective and average Eu-O bond distances has been calculated based on structural information gained from synchrotron powder diffraction data, but no clear evolution of this bond distances could be depicted (see Fig. S8). Using this model, the crystal field splitting, assumed to only depend on bond lengths in our system, cannot explain the observed blue shift of the excitation spectra. Besides the  $\text{Eu}^{2+}$  bond distances, the centroid shift variation is also dependent of the spectroscopic polarizability ( $\alpha_{\text{sp}}$ ) that is proportional to the inverse electronegativity value. The evolution of the spectroscopic polarizability has been studied based on the Allred-Rochow electronegativity scale (see Fig. S9) and shows a constant decrease along the solid solution, which is consistent with the observed variation toward higher energy of the centroid shift.

Experimental luminescence quenching energy determination combined with band gap theoretical calculations can be useful to

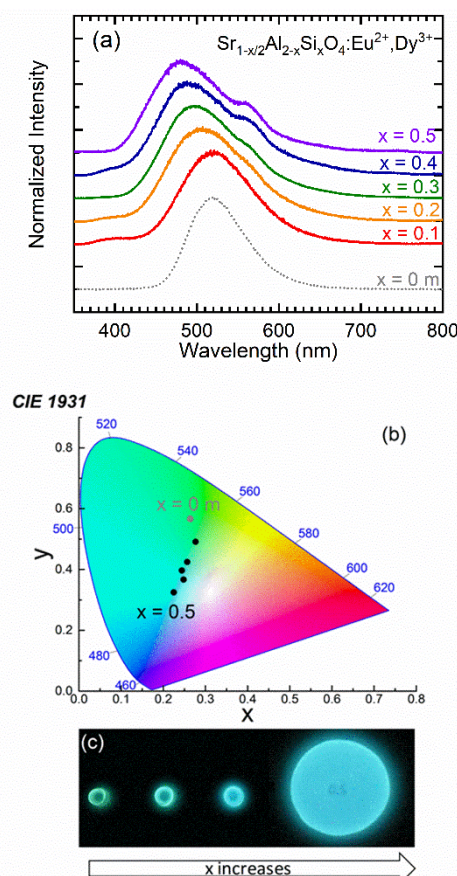


**Fig. 6.** (a) Persistent luminescence spectra of monoclinic  $x = 0$  (bottom) and hexagonal  $x = 0.1$  to  $x = 0.5$  (top) with  $\lambda_{\text{exc}} = 365$  nm for 5 min. (b) CIE coordinates of the persistent emission of the  $\text{Sr}_{1-x/2}\text{Al}_{2-x}\text{Si}_2\text{O}_4$  doped with 1 %  $\text{Eu}^{2+}$  and 2 %  $\text{Dy}^{3+}$ . (c) Pictures of the transparent ceramics taken after switching off the 365 nm excitation.



get insights on the evolution of the host band gap energy, and its relative position regarding the traps and recombination centres energy positions which are of major importance to study the trapping and de-trapping properties.

The thermal quenching of the  $\text{Eu}^{2+}$  emission, that may provide information about the energy difference between the  $\text{Eu}^{2+}$  excited state and the bottom of the conduction band, has been investigated. Figure 4 shows the integrated  $\text{Eu}^{2+}$  peak area of  $\text{Sr}_{1-x/2}\text{Al}_{2-x}\text{Si}_x\text{O}_4:\text{Eu}^{2+}$  ( $x$  ranging from 0.2 to 0.5) as a function of the sample temperature. It can be observed that the thermal quenching decreases when  $x$  increases. Indeed, the temperature at which the emission intensity is divided by two compared to the low temperature intensity, *i.e.* the quenching temperature ( $T_{1/2}$ ), varies from *ca.* 210 K to 295 K (for  $x = 0.2$  to 0.5 respectively). Assuming that, as previously reported<sup>59</sup> the relaxation towards the conduction band is responsible for thermal quenching, the energy difference between the excited  $\text{Eu}^{2+}$  5d state and the conduction band may increase with the Si substitution for Al.

Even though DFT calculations cannot provide accurate band gap energy values, it can be useful to depict a general tendency. For the hexagonal  $\text{SrAl}_2\text{O}_4$  and  $\text{Sr}_{1-x/2}\text{Al}_{2-x}\text{Si}_x\text{O}_4$  materials, the  $P6_322$  and  $P6_2c$  space groups have been used respectively, the related lattices are displayed in Figure 1(b) and (c). As presented in Fig. S10, along the  $\text{Sr}_{1-x/2}\text{Al}_{2-x}\text{Si}_x\text{O}_4$  solid solution, a general decrease of the band gap energy can be obtained. Figure 5 displays the relative orbitals contribution to the conduction band versus Si content. It can be observed that in the case of pure hexagonal  $\text{SrAl}_2\text{O}_4$ , the bottom of the conduction band is mainly composed of Sr 4d orbitals. Along the solid solution, an increasing contribution of (Al,Si) 3p orbitals appears. The bottom of the conduction band nature will further be used to discuss on the trap level position evolution.

### 3.3. Afterglow properties

Despite its interesting luminescence properties that enable to tune the  $\text{Sr}_{1-x/2}\text{Al}_{2-x}\text{Si}_x\text{O}_4$  materials emission,  $\text{Dy}^{3+}$  was originally used as a co-dopant aiming at obtaining new materials with enhanced persistent luminescence properties, as it is the best co-dopant reported for this purpose regarding monoclinic  $\text{SrAl}_2\text{O}_4:\text{Eu}^{2+}$ .<sup>6,7,9,11</sup> Figure 6(a) displays the afterglow emission spectra of h-SASO  $x$  co-doped samples. For  $x = 0$  monoclinic material, the well-known broad green band persistent luminescence is observed. In the case of the hexagonal phase, as for  $x = 0.1$ , the signal appears broadened. Then, similarly to steady state PL, the afterglow emission shifts towards lower

wavelengths along the solid solution. Again, this shift is due to structural changes in the  $\text{Eu}^{2+}$  surrounding. Interestingly, while keeping the same  $\text{Dy}^{3+}$  content in the materials, persistent emission of  $\text{Dy}^{3+}$  is also observable. Then, in the same way as observed for PL, the  $\text{Dy}^{3+}$  emission becomes more and more pronounced as the Si content increases, in particular at 573 nm.

The interesting point here is that the combination of these two phenomena leads to the afterglow colour change in the studied samples. The  $\text{Eu}^{2+}$  emission goes from green to blue and is combined to the increasing  $\text{Dy}^{3+}$  persistent emission in a yellow range, which overall results in a light blue persistent emission as the Si content increases. This is perfectly illustrated by the afterglow CIE (Commission Internationale de l'Eclairage) diagram reported in Figure 6(b). The observable colour shift of the materials persistent emission is displayed on the picture (see Figure 6(c)) on which the samples with  $x \geq 0.4$ , presents light blue persistent luminescence. Therefore, the glass crystallization synthesis process appears to be of great interest for possible further developments of large-scale transparent materials with tuneable persistent luminescence properties.

In the previous section, the persistent luminescence spectra have been recorded after charging using UV light. Afterwards, persistent excitation spectra, presented in Figure 7 (a), have been studied in order to find excitation wavelength ranges that enable persistent luminescence emission. In particular, the possibility to use visible light to charge persistent luminescence was attentively investigated. In the studied materials, all the persistent luminescence excitation spectra exhibit a large band extending up to 500 nm with a maximum at about 400 nm and a shoulder at about 250 nm. This observation reveals an interesting possible charging of the light blue persistent luminescence by exciting the transparent materials with blue light. The shape of the afterglow excitation spectra is remarkably similar to the steady state excitation spectra of the samples. Indeed, increasing  $x$  leads to a very slight blue shift of the excitation band as well as an increase of the UV band. This clearly indicates that the charging pathway goes through the  $\text{Eu}^{2+}$  4f  $\rightarrow$  5d excitation bands. To evaluate the possible visible light activation of persistent luminescence in h-SASO 0.5, persistent luminescence spectra and glow curves have been measured after one-minute excitation using a typical smartphone white LED. The integrated afterglow decay curve, as well as the related afterglow spectra, are displayed in Figure 7(b). Interestingly, the light blue afterglow remains for minutes, even after this white LED charging with relatively weak irradiation power and time. This behaviour could be of major interest for further indoor security signage applications.

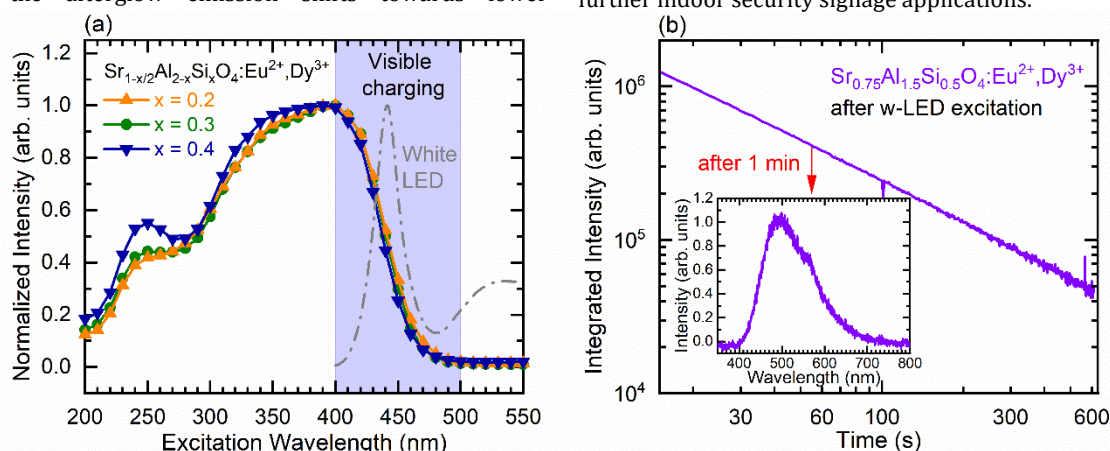


**Fig. 7.** (a) Persistent luminescence excitation spectra ( $\lambda_{\text{em}} = 488$  nm for  $x = 0.2$  and  $\lambda_{\text{em}} = 478$  nm for  $x > 0.2$ ). (b) Persistent luminescence decay of the  $x = 0.5$  sample after mobile phone w-LED charging. The persistent emission spectrum is displayed in the inset.

The persistent luminescence decay curves of the co-doped  $\text{Sr}_{1-x/2}\text{Al}_{2-x}\text{Si}_x\text{O}_4$  materials are displayed in Figure 8(a). Even though the monoclinic  $\text{SrAl}_2\text{O}_4:\text{Eu}^{2+},\text{Dy}^{3+}$  material, prepared with the same experimental method, shows the highest radiance decay, the decay profiles of all the samples are in a same order of magnitude. This indicates the efficient persistent luminescence properties of the  $\text{Sr}_{1-x/2}\text{Al}_{2-x}\text{Si}_x\text{O}_4:\text{Eu}^{2+},\text{Dy}^{3+}$  ceramics. Interestingly, a higher  $\text{Si}^{4+}$  for  $\text{Al}^{3+}$  substitution content leads to a more intense persistent luminescence signal. This means that the material with the higher Si content enables a more favourable charge de-trapping at room temperature. The comparison of  $\text{Eu}^{2+}$  and  $\text{Dy}^{3+}$  persistent decays, plotted in Fig. S11, shows that the  $\text{Dy}^{3+}$  persistent decay follows the same slope as  $\text{Eu}^{2+}$ . It reveals that they might follow the same persistent luminescence mechanism. After being un-trapped, the charges may recombine on  $\text{Eu}^{2+}$  excited state and a partial energy transfer to  $\text{Dy}^{3+}$  can happen.

The most common analysis technique used to study persistent luminescence materials and charge trapping is thermoluminescence. Low temperature thermoluminescence of the studied materials are presented in Figure 8(b) and (c) while the thermoluminescence glow curves of the h-SASO  $x = 0.5$  sample recorded after charging at 273 K and 13 K is presented in Figure S12. Comparison of the TL intensities between low and room temperature charging evidences the thermal activation of the persistent luminescence charging as previously reported<sup>58</sup> whereas the comparison of glow curves shape gives insights on the complete trap depth distribution as seen in figure 8. Indeed, charging at 273 K, the observation of shallow traps is vanished, making difficult the full traps comparison in the different samples as expressed in figures 8(b)-(c). TL intensity of the different samples around room temperature appears to be in good agreement with their related afterglow decay curves. Looking at the TL glow curves shape reported figure 8; it can be observed that at least two kinds of traps at different depths are involved in the persistent luminescence mechanism. Indeed, for all samples, two broad bands can be distinguished. As the Si content increases, the TL bands shift towards higher temperatures, and in this case become closer to room temperature, which is of large interest from persistent luminescence applications point of view. The shift of the TL peaks towards higher temperatures reveals an increase of the activation energy of the involved traps. This means that in the classic case where electrons are trapped close to the conduction band, the energy of the lowest conduction band level should increase regarding the traps levels. This is in good agreement with the thermal quenching studied previously in samples containing different Si contents and also provides important clues for mechanism determination. The thermoluminescence glow curve of the powdered  $\text{SrAl}_2\text{O}_4:\text{Eu}^{2+},\text{Dy}^{3+}$  sample, obtained with the ADL method, displayed in Fig. S13, is relatively narrow and centred around 275 K. Therefore, the involved traps are indeed less energy dispersed than those of h-SASO 0.5. These features can explain that the persistent luminescence decay of the powdered  $\text{SrAl}_2\text{O}_4:\text{Eu}^{2+},\text{Dy}^{3+}$  sample is initially more intense (in the first seconds) but also steeper compared to the h-SASO 0.5 one, as observed in Fig. 8 (a).

Nevertheless, the role of  $\text{Dy}^{3+}$  in the charge trapping mechanism is intriguing. In order to gain deeper insights on the traps nature, samples with different  $\text{Dy}^{3+}$  contents (from 0 % to 5 %) have been prepared and studied in a similar way. Firstly, both TL peaks vary when the  $\text{Dy}^{3+}$  doping content varies. Interestingly, it is noticeable that the two TL peaks are observable with all different  $\text{Dy}^{3+}$  doping contents, even when the sample is only doped by  $\text{Eu}^{2+}$  (single doping). As no additional peak appears when  $\text{Dy}^{3+}$  is added, this means that  $\text{Dy}^{3+}$  should not behave as a direct trap. On

the other hand, the low temperature glow peak increases drastically when  $\text{Dy}^{3+}$  is added. This reveals that  $\text{Dy}^{3+}$  may stabilize the shallow traps. Moreover, this low temperature glow peak appears to shift towards higher temperatures as the  $\text{Dy}^{3+}$  content increases. This means that the related trap depth increases when  $\text{Dy}^{3+}$  is added, revealing a higher energy stability of the involved defects. This result is in agreement with the persistent luminescence mechanism proposed by Clabau *et al.*<sup>9,60,61</sup> where hypothesis of the defect nature according to the reducing atmosphere used for samples preparation could be some oxygen vacancies. This is also in good agreement with previous works of J. Hölsä and co-workers in which experimental and theoretical results highlighted the importance of intrinsic oxygen vacancies in the room temperature persistent luminescence mechanism and the ability of  $\text{RE}^{3+}$  co-dopant to increase the storage capability.<sup>62–65</sup>

In the  $\text{SrAl}_2\text{O}_4$  case, the localized energy levels created by oxygen vacancies can be seen as an empty aluminium  $\text{sp}^3$  orbital. From a molecular orbital point of view, it can be seen as the transition

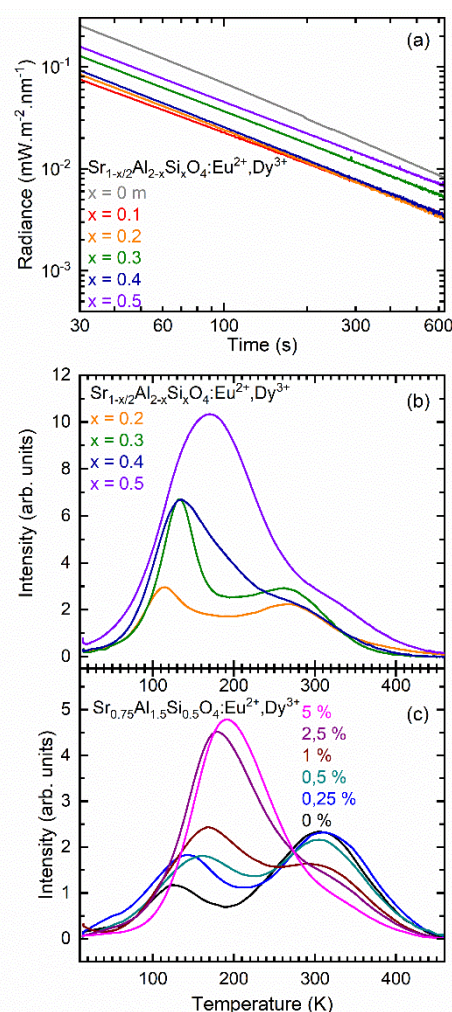


**Fig. 8.** (a) Comparison of the radiance decay curves and (b) thermoluminescence of  $\text{Sr}_{1-x/2}\text{Al}_{2-x}\text{Si}_x\text{O}_4$  transparent ceramics doped with 1%  $\text{Eu}^{2+}$  and 2%  $\text{Dy}^{3+}$  after  $\lambda_{\text{exc}} = 365$  nm for 5 min at 13 K. For sake of comparison, the radiance decay curve of the monoclinic  $\text{SrAl}_2\text{O}_4$  doped and prepared with the same process is presented. Notice that experiments were done on powder samples. (c) Thermoluminescence glow curves of  $\text{Sr}_{0.75}\text{Al}_{1.5}\text{Si}_{0.5}\text{O}_4:\text{Eu}^{2+}$  with different  $\text{Dy}^{3+}$  doping contents (0, 0.25, 0.5, 1, 2.5 and 5 %)  $\lambda_{\text{exc}} = 365$  nm for 5 min at 13 K.

from  $[\text{AlO}_4]^{5-}$  (Td) to  $[\text{AlO}_3]^{4-}$  (C<sub>3v</sub>), leading to a splitting of the Al



3p antibonding energy level, which can be seen as the LUMO.<sup>66,67</sup> Along the solid solution, part of  $[\text{AlO}_4]^{5-}$  tetrahedron are replaced by  $[\text{SiO}_4]^{4-}$  tetrahedron. As the Si-O bond strength is generally larger compared to Al-O one due to its higher electronegativity, this may induce a higher energy level splitting between the  $6a_1^*$  stabilized and  $4e^*$  not stabilized level, *i.e.* a higher trap depth, that is indeed observed on the main trap peak position on the thermoluminescence glow curves.

On the other hand, the TL intensity of the peak close to room temperature decreases. In a practical point of view, this evidences less intense decay curves and persistent luminescence intensity when  $\text{Dy}^{3+}$  increases. This has been confirmed with persistent glow curves (Fig. S14) in which the intensity of the glow curves decreases with the  $\text{Dy}^{3+}$  doping concentration. Still, the intensity of the glow curves of the different samples is in the same order of magnitude, as previously observed for TL intensities. This reveals that the incorporation of more defect-stabilizing doping ion, enables slightly deeper trap depths, suitable for room temperature relaxation that can significantly improve the persistent intensity of studied transparent ceramic phosphors. This is promising insight in improving the afterglow performance of studied samples.

## 4. Conclusions

Transparent persistent phosphors belonging to the hexagonal  $\text{Sr}_{1-x/2}\text{Al}_{2-x}\text{Si}_x\text{O}_4:\text{Eu}^{2+},\text{Dy}^{3+}$  solid-solution were obtained by full glass crystallization. The synthesis conditions, using (i) a double  $\text{CO}_2$  laser heating system coupled to an aerodynamic levitation to ensure glass forming and then (ii) a single heat treatment to perform full crystallization, enable to obtain transparent ceramic monoliths for a large composition range, from  $x = 0.1$  to  $x = 0.5$ . In addition, glass formation of the  $\text{Eu}^{2+}, \text{Dy}^{3+}$  co-doped  $\text{Sr}_{0.75}\text{Al}_{1.5}\text{Si}_{0.5}\text{O}_4$  composition ( $x = 0.5$ ) can be achieved in a regular commercial furnace using a platinum/rhodium crucible. It is therefore possible to scale up the process and synthesize large transparent ceramic pieces. The  $\text{Sr}_{1-x/2}\text{Al}_{2-x}\text{Si}_x\text{O}_4:\text{Eu}^{2+},\text{Dy}^{3+}$  ceramics demonstrate a colour shift varying from green to light blue (from  $x = 0.1$  to  $x = 0.5$ ) from both steady state photoluminescence and persistent luminescence measurements. This colour change is assigned to a blue shift of the  $\text{Eu}^{2+} 5d \rightarrow 4f$  emission and to the appearance of  $\text{Dy}^{3+}$  emission lines. In addition to this colour evolution, materials with increasing Si contents exhibit longer persistent decays. Persistent luminescence excitation results show that a broad range of wavelength, extending from UV to blue/green light, can effectively charge the persistent materials and that charging with low power white LEDs, as those available in mobile phones, is sufficient to observe the blueish white persistent emission for several tens of minutes. Finally, the temperature dependence of photoluminescence, thermoluminescence and DFT calculations provide insights about the evolution of the persistent luminescence properties as the Si content increases and the trap depths become deeper hence closer to optimal trap depth position for persistent luminescence.

$\text{Eu}^{2+},\text{Dy}^{3+}$  doped  $\text{Sr}_{1-x/2}\text{Al}_{2-x}\text{Si}_x\text{O}_4$  fulfil all the three criteria (transparency and the related volume effect, tuneable persistent luminescence, possible charging with visible light) to be suitable for night lighting applications. However, an enhancement of persistent intensity is still required to move towards commercial development, and our results suggest that promising improvements by suitable codopants can be realized.

## Conflicts of interest

There are no conflicts of interest to declare.

## Acknowledgements

The French Research Council is acknowledged for financial support within PSL, the ANR, ANR-18-CE08-0012 PERSIST and CNRS PICS Program. J. Xu, K. Asami and S. Tanabe acknowledge financial supports by the Grant-in-Aid for JSPS Fellows (No. 18F18051) and JSPS Grant-in-Aid for Scientific Research on Innovative Areas "Mixed anion" (No. JP16H6441). A. J. Fernández-Carrión thanks the National Natural Science Foundation of China (No. 21850410458) for the financial support.

## References

1. Matsuzawa, T. A New Long Phosphorescent Phosphor with High Brightness,  $\text{SrAl}_2\text{O}_4:\text{Eu}^{2+},\text{Dy}^{3+}$ . *Journal of The Electrochemical Society* **143**, 2670 (1996).
2. Hisako Takasaki, Tanabe, S. & Hanada, T. Long-Lasting Afterglow Characteristics of Eu, Dy Codoped  $\text{SrO-Al}_2\text{O}_3$  Phosphor. *Journal of the Ceramic Society of Japan* 322–326 (1996).
3. Katsumata, T., Nabae, T., Sasajima, K. & Matsuzawa, T. Growth and characteristics of long persistent  $\text{SrAl}_2\text{O}_4$ - and  $\text{CaAl}_2\text{O}_4$ -based phosphors crystals by a floating zone technique.
4. Nakanishi, T. *et al.* Fabrication of  $\text{Eu}:\text{SrAl}_2\text{O}_4$ -based glass ceramics using Frozen sorbet method. *Journal of the Ceramic Society of Japan* **119**, 609–615 (2011).
5. Peng, T. *et al.* Combustion synthesis and photoluminescence of  $\text{SrAl}_2\text{O}_4:\text{Eu},\text{Dy}$  phosphor nanoparticles. *Materials Letters* **58**, 352–356 (2004).
6. Zhang, T. & Su, Q. Rare-earth materials for use in the dark. *Journal of the Society for Information Display* **8**, 27 (2000).
7. Aitasalo, T. *et al.* Persistent luminescence phenomena in materials doped with rare earth ions. *Journal of Solid State Chemistry* **171**, 114–122 (2003).
8. Aitasalo, T. *et al.* Annihilation of the persistent luminescence of  $\text{MgAl}_2\text{O}_4:\text{Eu}^{2+}$  by  $\text{Sm}^{3+}$  co-doping. *Radiation Measurements* **38**, 515–518 (2004).
9. Clabau, F. *et al.* Mechanism of Phosphorescence Appropriate for the Long-Lasting Phosphors  $\text{Eu}^{2+}$ -Doped  $\text{SrAl}_2\text{O}_4$  with Codopants  $\text{Dy}^{3+}$  and  $\text{B}^{3+}$ . *Chemistry of Materials* **17**, 3904–3912 (2005).
10. Niittykoski, J. *et al.* Effect of boron substitution on the preparation and luminescence of  $\text{Eu}^{2+}$  doped strontium aluminates. *Journal of Alloys and Compounds* **374**, 108–111 (2004).
11. Aitasalo, T. *et al.* Low temperature thermoluminescence properties of  $\text{Eu}^{2+}$  and  $\text{R}^{3+}$  doped  $\text{CaAl}_2\text{O}_4$ . *Journal of Alloys and Compounds* **380**, 4–8 (2004).
12. Aitasalo, T., Hölsä, J., Jungner, H., Lastusaari, M. & Niittykoski, J. Thermoluminescence Study of Persistent Luminescence Materials:  $\text{Eu}^{2+}$ - and  $\text{R}^{3+}$ -Doped Calcium Aluminates,  $\text{CaAl}_2\text{O}_4:\text{Eu}^{2+},\text{R}^{3+}$ . *The Journal of Physical Chemistry B* **110**, 4589–4598 (2006).
13. Korthout, K. *et al.* Luminescence and x-ray absorption measurements of persistent  $\text{SrAl}_2\text{O}_4:\text{Eu},\text{Dy}$  powders: Evidence for valence state changes. *Physical Review B* **84**, (2011).
14. Ueda, J., Nakanishi, T., Katayama, Y. & Tanabe, S. Optical and optoelectronic analysis of persistent luminescence in  $\text{Eu}^{2+}-\text{Dy}^{3+}$  codoped  $\text{SrAl}_2\text{O}_4$  ceramic phosphor: Optical and optoelectronic analysis of persistent luminescence in  $\text{Eu}^{2+}-\text{Dy}^{3+}$  codoped  $\text{SrAl}_2\text{O}_4$  ceramic phosphor. *Phys. Status Solidi C* **9**, 2322–2325 (2012).
15. Xu, J. & Tanabe, S. Persistent luminescence instead of phosphorescence: History, mechanism, and perspective. *Journal of Luminescence* **205**, 581–620 (2019).
16. Van den Eeckhout, K., Smet, P. F. & Poelman, D. Persistent Luminescence in  $\text{Eu}^{2+}$ -Doped Compounds: A Review. *Materials* **3**, 2536–2566 (2010).

17. Van den Eeckhout, K., Poelman, D. & Smet, P. Persistent Luminescence in Non-Eu<sup>2+</sup>-Doped Compounds: A Review. *Materials* **6**, 2789–2818 (2013).
18. Ueda, J., Kuroishi, K. & Tanabe, S. Yellow persistent luminescence in Ce<sup>3+</sup>–Cr<sup>3+</sup>-codoped gadolinium aluminum gallium garnet transparent ceramics after blue-light excitation. *Applied Physics Express* **7**, 062201 (2014).
19. Xu, J., Ueda, J., Kuroishi, K. & Tanabe, S. Fabrication of Ce<sup>3+</sup>–Cr<sup>3+</sup>-co-doped yttrium aluminium gallium garnet transparent ceramic phosphors with super long persistent luminescence. *Scripta Materialia* **102**, 47–50 (2015).
20. Boutinaud, P., Sarakha, L. & Mahiou, R. NaNbO<sub>3</sub>:Pr<sup>3+</sup>: a new red phosphor showing persistent luminescence. *J. Phys.: Condens. Matter* **21**, 025901 (2009).
21. Boutinaud, P. *et al.* About red afterglow in Pr<sup>3+</sup> doped titanate perovskites. *J. Phys. D: Appl. Phys.* **42**, 045106 (2009).
22. Li, L. *et al.* Tunable Trap Depth for Persistent Luminescence by Cationic Substitution in Pr<sub>3-x</sub>K<sub>x</sub>NbO<sub>3</sub> Perovskites. 2629–2639 (2019).
23. Maldiney, T. *et al.* The in vivo activation of persistent nanophosphors for optical imaging of vascularization, tumours and grafted cells. *Nature Mater* **13**, 418–426 (2014).
24. Allix, M. *et al.* Considerable Improvement of Long-Persistent Luminescence in Germanium and Tin Substituted ZnGa<sub>2</sub>O<sub>4</sub>. *Chemistry of Materials* **25**, 1600–1606 (2013).
25. Castaing, V. *et al.* Persistent Luminescence of ZnGa<sub>2</sub>O<sub>4</sub>:Cr<sup>3+</sup> Transparent Glass Ceramics: Effects of Excitation Wavelength and Excitation Power. 5114–5120 (2017).
26. Pan, Z. *et al.* Facilitating Low-Energy Activation in the Near-Infrared Persistent Luminescent Phosphor Zn<sub>1+x</sub>Ga<sub>2-x</sub>Sn<sub>x</sub>O<sub>4</sub>:Cr<sup>3+</sup> via Crystal Field Strength Modulations. 8347–8358 (2020).
27. <https://www.bbc.com/news/technology-27021291>.
28. [https://www.huffpost.com/entry/glow-in-dark-bike-path-lane-sun-poland\\_n\\_57fd0732e4b068ecb5e1d57b](https://www.huffpost.com/entry/glow-in-dark-bike-path-lane-sun-poland_n_57fd0732e4b068ecb5e1d57b).
29. Zhuang, Y., Ueda, J. & Tanabe, S. Multi-color persistent luminescence in transparent glass ceramics containing spinel nano-crystals with Mn<sup>2+</sup> ions. *Applied Physics Letters* **105**, 191904 (2014).
30. Xu, J., Tanabe, S., Sontakke, A. D. & Ueda, J. Near-Infrared Multi-Wavelengths Long Persistent Luminescence of Nd<sup>3+</sup> Ion Through Persistent Energy Transfer in Ce<sup>3+</sup>, Cr<sup>3+</sup> Co-Doped Y<sub>3</sub>Al<sub>2</sub>Ga<sub>3</sub>O<sub>12</sub> for the First and Second Bio-Imaging Windows. 081903 (2015).
31. Castaing, V. *et al.* Persistent Energy Transfer in ZGO:Cr<sup>3+</sup>,Yb<sup>3+</sup> a New Strategy to Design Nano Glass-Ceramics Featuring Deep Red and Near Infrared Persistent Luminescence. *Physical Chemistry Chemical Physics* 19458–19468 (2019).
32. Gandhi, A. S., Saravanan, A. & Jayaram, V. Containerless processing of ceramics by aerodynamic levitation. *Materials Science and Engineering: A* **221**, 68–75 (1996).
33. Allix, M. *et al.* Highly Transparent BaAl<sub>4</sub>O<sub>7</sub> Polycrystalline Ceramic Obtained by Full Crystallization from Glass. *Adv. Mater.* **24**, 5570–5575 (2012).
34. Alahraché, S. *et al.* Perfectly Transparent Sr<sub>3</sub>Al<sub>2</sub>O<sub>6</sub> Polycrystalline Ceramic Elaborated from Glass Crystallization. *Chem. Mater.* **25**, 4017–4024 (2013).
35. Al Saghir, K. *et al.* Transparency through Structural Disorder: A New Concept for Innovative Transparent Ceramics. *Chem. Mater.* **27**, 508–514 (2015).
36. Saghir, K. A. Transparent ceramics by full crystallization from glass: application to strontium aluminosilicates. 314.
37. Boyer, M. *et al.* Enhanced Transparency through Second Phase Crystallization in BaAl<sub>4</sub>O<sub>7</sub> Scintillating Ceramics. *Crystal Growth & Design* **16**, 386–395 (2016).
38. Boyer, M. *et al.* Transparent polycrystalline SrREGa<sub>3</sub>O<sub>7</sub> melilite ceramics: potential phosphors for tuneable solid state lighting. *J. Mater. Chem. C* **4**, 3238–3247 (2016).
39. Boyer, M. *et al.* First transparent oxide ion conducting ceramics synthesized by full crystallization from glass. *J. Mater. Chem. A* 5276–5289 (2018).
40. Ma, X. *et al.* Pressureless glass crystallization of transparent yttrium aluminum garnet-based nanoceramics. *Nat Commun* **9**, 1175 (2018).
41. Bertrand, A. *et al.* Scalable and Formable Tellurite-Based Transparent Ceramics for Near Infrared Applications. 1482 (2016).
42. Fernandez-Carrion, A. J. *et al.* Local Disorder and Tunable Luminescence in Sr<sub>1-x/2</sub>Al<sub>2-x</sub>Si<sub>x</sub>O<sub>4</sub> (0.2 ≤ x ≤ 0.5) Transparent Ceramics. *Inorganic Chemistry* **56**, 14446–14458 (2017).
43. Wisniewski, W., Fernández-Carrión, A. J., Schöppe, P., Rüssel, C. & Allix, M. Oriented nucleation and crystal growth in SrO–Al<sub>2</sub>O<sub>3</sub>–SiO<sub>2</sub> tectosilicate glasses. *CrystEngComm* **20**, 3455–3466 (2018).
44. Shinozaki, K., Honma, T., Affatigato, M. & Komatsu, T. Long Afterglow in Hexagonal SrAl<sub>2</sub>O<sub>4</sub>:Eu<sup>2+</sup>, Dy<sup>3+</sup> Synthesized by Crystallization of Glass and Solidification of Supercooled Melts. 286–289 (2016).
45. Poort, S. H. M., Blokpoel, W. P. & Blasse, G. Luminescence of Eu<sup>2+</sup> in barium and strontium aluminate and gallate. *Chemistry of Materials* **7**, 1547–1551 (1995).
46. Winborne, D. A., Nordine, P. C., Rosner, D. E. & Marley, N. F. Aerodynamic levitation technique for containerless high temperature studies on liquid and solid samples. *MTB* **7**, 711–713 (1976).
47. Weber, J. K. R. The Containerless Synthesis of Glass: The Containerless Synthesis of Glass. *International Journal of Applied Glass Science* **1**, 248–256 (2010).
48. Clark, S. J. *et al.* First principles methods using CASTEP. *Zeitschrift für Kristallographie - Crystalline Materials* **220**, (2005).
49. Perdew, J. P., Burke, K. & Ernzerhof, M. Generalized Gradient Approximation Made Simple. *Phys. Rev. Lett.* **77**, 3865–3868 (1996).
50. Vanderbilt, D. Soft self-consistent pseudopotentials in a generalized eigenvalue formalism. *Phys. Rev. B* **41**, 7892–7895 (1990).
51. Koelling, D. D. & Harmon, B. N. A technique for relativistic spin-polarised calculations. *Journal of Physics C* **10**, 3107 (1977).
52. Shannon, R. D. Revised Effective Ionic Radii and Systematic Studies of Interatomic Distances in Halides and Chalcogenides. 751–767 (1976).
53. Schulze, A.-R. & Buschbaum, Hk. M. Zur Verbindungsbildung von MeO: M<sub>2</sub>O<sub>3</sub>. IV. Zur Struktur von monoklinem SrAl<sub>2</sub>O<sub>4</sub>. *Zeitschrift für anorganische und allgemeine Chemie* **475**, 205–210 (1981).
54. Dorenbos, P. Energy of the first 4f<sup>7</sup>→4f<sup>6</sup>5d transition of Eu<sup>2+</sup> in inorganic compounds. *Journal of Luminescence* **104**, 239–260 (2003).
55. Dorenbos, P. Relation between Eu<sup>2+</sup> and Ce<sup>3+</sup> f d-transition energies in inorganic compounds. *J. Phys.: Condens. Matter* **15**, 4797–4807 (2003).
56. Dorenbos, P. Crystal field splitting of lanthanide 4f<sub>n</sub>215d-levels in inorganic compounds. *Journal of Alloys and Compounds* **4** (2002).
57. Dorenbos, P., Andriessen, J. & van Eijk, C. W. E. 4 f<sub>n</sub>–1 5 d centroid shift in lanthanides and relation with anion polarizability, covalency, and cation electronegativity. *Journal of Solid State Chemistry* **171**, 133–136 (2003).
58. Botterman, J., Joos, J. J. & Smet, P. F. Trapping and detrapping in SrAl<sub>2</sub>O<sub>4</sub>:Eu, Dy persistent phosphors: Influence of excitation wavelength and temperature. *Phys. Rev. B* **90**, 085147 (2014).
59. Dorenbos, P. Thermal quenching of Eu<sup>2+</sup> 5d–4f luminescence in inorganic compounds. *Journal of Physics: Condensed Matter* **17**, 8103–8111 (2005).
60. Clabau, F. *et al.* On the phosphorescence mechanism in SrAl<sub>2</sub>O<sub>4</sub>:Eu<sup>2+</sup> and its codoped derivatives. *Solid State Sciences* **9**, 608–612 (2007).
61. Clabau, F. *et al.* Fluorescence and phosphorescence properties of the low temperature forms of the MAl<sub>2</sub>Si<sub>2</sub>O<sub>8</sub>:Eu<sup>2+</sup> (M=Ca, Sr, Ba) compounds. *Journal of Solid State Chemistry* **181**, 1456–1461 (2008).
62. Carlson, S. *et al.* X-ray absorption study of rare earth ions in Sr<sub>2</sub>MgSi<sub>2</sub>O<sub>7</sub>:Eu<sup>2+</sup>,R<sup>3+</sup> persistent luminescence materials. *Optical Materials* **31**, 1877–1879 (2009).
63. Hölsä, J. *et al.* Valence and environment of rare earth ions in CaAl<sub>2</sub>O<sub>4</sub>:Eu<sup>2+</sup>,R<sup>3+</sup> persistent luminescence materials. *Spectrochimica Acta Part B: Atomic Spectroscopy* **65**, 301–305 (2010).
64. Brito, H. F. *et al.* Optical energy storage properties of Sr<sub>2</sub>MgSi<sub>2</sub>O<sub>7</sub>:Eu<sup>2+</sup>,R<sup>3+</sup> persistent luminescence materials. *J Therm Anal Calorim* **105**, 657–662 (2011).

65. Hölsä, J., Laamanen, T., Lastusaari, M. & Novák, P. Isolated Defects in Sr<sub>2</sub>MgSi<sub>2</sub>O<sub>7</sub>: A DFT Study. *Physics Procedia* **29**, 76–85 (2012).
66. Clabau, F. Phosphorescence : mécanismes et nouveaux matériaux. (2005).
67. Lecointre, A. Mécanisme de luminescence persistante de nouveaux types de marqueurs pour l'imagerie optique in vivo. (2010).